RSC Advances

PAPER

View Article Online
View Journal | View Issue

Cite this: *RSC Adv.*, 2024, **14**, 13801

Molecular engineering to design a bright near-infrared red photosensitizer: cellular bioimaging and phototherapy†

Zhiyong Li,‡[a] Yili Xie,‡[b] Heng Liu,‡[e] Jing Wang,[c] Gang Wang,[e] Hengxin Wang,[e] Xuejie Su,[e] Meixu Lei,[e] Qing Wan,[f] Yali Zhou*[d] and Muzhou Teng*[e]

Near-infrared red (NIR) fluorescence imaging guide phototherapeutic therapy (PDT) has the advantages of deep tissue penetration, real-time monitoring of drug treatment and disease, little damage to normal tissue, low cytotoxicity and almost no side effects, and thus, it is attracting increasing research attention and is expected to show promising potential for clinical tumor treatment. The photosensitizer (PS), light source and oxygen are the three basic and important factors to construct PDT technology, and highly efficient PSs are still being passionately pursued because they determine the PDT efficiency. Ideal PSs should have properties such as good biocompatibility, deep tissue penetration, and highly efficient reactive oxygen species (ROS) generation despite the hypoxic environment. Therefore, pure organic type I PSs with NIR fluorescence have been receiving increasing attention due to their deep penetration and hypoxia resistance. However, reported NIR-active type I PSs usually require complex synthetic procedures, which presents a challenge for mass production. In this research work, based on the molecular design ideas of introducing the heavy atom effect and intramolecular charge transfer, we prepared three NIR-active type I PSs (TNZ, TNZBr, and TNZCHO) using a very simple method with one or two synthetic steps. Clear characterizations of photophysical properties, ROS performance tests, and fluorescent imaging of human umbilical vein endothelial (HUVE) cells and PDT treatment of HepG2 cells were carried out. The results revealed that the heavy atom and intramolecular charge transfer (ICT) effects could obviously enhance the ROS efficiency, and both PSs produce only type I ROS without any type II ROS ($^1O_2$) generation. The good NIR fluorescence brightness and type I ROS efficiency ensure satisfactory bioimaging and PDT outcomes. This research provides the possibility of preparing NIR-active type I PSs *via* mass production.

Received 5th February 2024
Accepted 11th April 2024

DOI: 10.1039/d4ra00928b

rsc.li/rsc-advances

Introduction

Cancer and bacterial infections are serious threats to the health and safety of human beings.[1] Although traditional drug therapy can effectively suppress tumor growth and provide resistance to bacterial infections, the emergence of drug-resistance and cytotoxic side effects of chemotherapy hinder their clinical treatment effect,[2,3] which has driven researchers to pursue safer therapeutic methods that can retain great therapeutic efficiency while minimizing drug resistance and toxic side effects. Photodynamic therapy (PDT) approaches are constructed using three important factors, namely, a photosensitizer (PS), photosource and oxygen, to generate cytotoxic reactive oxygen species (ROS) to destroy cellular/bacterial structures and induce death. PDT has the advantages of great therapeutic efficiency, little damage to normal tissue, low cytotoxicity and almost no side effects.[4–7]

Photosensitizers (PSs) are the core component to produce ROS under light irradiation, and their performances determine the efficiency in the PDT process of PDT. To meet the requirements of biological applications, ideal PSs should have the properties of water solubility, good biocompatibility, near-infrared red (NIR) absorption or emission wavelengths, and highly efficient ROS production ability.[8–10] Recently, increasing research attention has been paid to the development of

[a]*Vascular Surgery Department, The Second Hospital & Clinical Medical School, Lanzhou University, Lanzhou, 730000, China*
[b]*College of Ecology and Environment, Yuzhang Normal University, Nanchang 330103, China*
[c]*Healthy Examination & Management Center, The Second Hospital & Clinical Medical School, Lanzhou University, Lanzhou, 730000, China*
[d]*Cuiying Biomedical Research Center, The Second Hospital & Clinical Medical School, Lanzhou University, Lanzhou, 730000, China*
[e]*The Second Hospital & Clinical Medical School, Lanzhou University, Lanzhou, 730000, China*
[f]*School of Materials Science and Engineering, Nanchang Hangkong University, Nanchang, 330063, China*

† Electronic supplementary information (ESI) available. See DOI: https://doi.org/10.1039/d4ra00928b

‡ The authors contributed equally to this work.

advanced organic PSs, which mainly include a series of derivatives based on porphyrin,[11] rhodamine,[12] and phthalocyanine units.[13] Although above-mentioned effective PSs could achieve satisfactory phototherapeutic outcomes towards tumors and bacteria, their weak fluorescence intensity as well as the reduced ROS efficiency caused by stronger intermolecular π–π stacking interactions are unfavorable for their application in fluorescence-imaging-guided PDT.[14,15] In contrast, new PSs with aggregation-induced emission (AIE) properties are usually constructed with a twisted molecular conformation that can effectively inhibit π–π stacking interactions to boost the fluorescence intensity and ROS efficiency.[16–18] Therefore, AIE-active PSs have recently received increasing research interest for the PDT of tumors and wound infections.[19,20] However, most AIE-active PSs mainly produce the type II ROS of singlet oxygen ($^1O_2$), which creates the challenge of reduced ROS efficiency in the tumor microenvironment due to the hypoxia effect of tumors. To overcome this problem, many innovative methods have been proposed, such as hyperbaric oxygen therapy to enhance oxygen perfusion in tumors and oxygen self-supplement systems to promote oxygen generation.[21,22] Although above-mentioned methods achieved outstanding effects in terms of relieve hypoxia, untoward side effects such as hyperoxic seizures and barotrauma problems from above-mentioned approaches were also reported. As an alternative to the oxygen supply method, creating PSs with low oxygen dependence might be a more promising research direction for the clinical application of PDT technology.

Unlike $^1O_2$, other ROS, such as the superoxide anion radical ($O_2^{\bullet-}$) and hydroxy radical ($OH^{\bullet}$), which are classified as type I ROS, have the property of low oxygen-dependence, thus showing promising application potential for hypoxic tumor treatment.[23] Recently, increasing research attention has been paid to the development of AIE-active PSs with type I ROS generation of $O_2^{\bullet-}$ and $OH^{\bullet}$, which show great bioimaging and PDT efficiency for hypoxic tumors because of their unique advantages of aggregation-enhanced fluorescence and ROS efficiency as well as low oxygen-dependence.[24,25] However, most of the reported type I PSs require complex synthetic processes, especially the type I PSs with near-infrared red (NIR) fluorescence, which are usually fabricated by designing complex molecular structures with a stronger intramolecular charge transfer state or longer electronic conjugation, present difficult synthetic and purification processes.[26] Therefore, developing new AIE-active type I PSs with NIR fluorescence that have the feature of simple synthetic steps is of special importance for promoting the clinical transformation of type I PDT technology.

In this work, we synthesized two different type I PSs with aggregation-induced NIR fluorescence *via* very simple one- or two-synthetic-step approaches. Naphtho(2,3-*c*)(1,2,5)thiadiazole (NTZ), which is usually used to fabricate deep-red and NIR emitters with improved molar absorption coefficients and photoluminescent quantum yields (PLQYs), was adopted as the research moiety.[27,28] To achieve AIE and NIR properties, the typical AIE-active electronic donor triphenylamine (TPA) was conjugated with one side of NTZ to obtain the compound TNZ as a reference, and a heavy atom (Br) and electron-withdrawing aldehyde group were introduced to the other side of NTZ to give the two new photosensitizers of TNZBr and TNZCHO (Scheme 1). Experimental results show that the introduction of the heavy atom and ICT effects would not only red-shift the emission maximum to the NIR region but also greatly improve their ROS efficiency. TNZCHO maintains good fluorescence intensity when aggregated, while the fluorescence is quenched for TNZBr. Detailed identification of ROS unexpectedly reveals that TNZBr and TNZCHO generate only the type I ROS $O_2^{\bullet-}$ and $OH^{\bullet}$ after white-light irradiation, and there is not any $^1O_2$ generation for these two PSs. Finally, we evaluate the fluorescent cellular imaging and PDT efficacy of these two PSs for human umbilical vein endothelial (HUVEC) cells and HepG2 cancer cells under normal oxygen and hypoxic conditions; the cellular viability is lower than 20% upon white light irradiation, indicating a satisfactory PDT outcome toward the cancer cells. Compared with the type I PSs reported recently,[29–36] the advantage of this work is providing a simple method to prepare free-radical PSs with deep red fluorescence. However, several shortcomings are also obvious; for example, the absorption and emission wavelengths do not reach the near-infrared red region, which is unfavorable for achieving excellent PDT outcomes in the deep tumor. In addition, the PSs should be endowed with activatable performance, which could effectively solve the problem of PS phototoxicity post-PDT.

Results and discussion

Synthesis and characterization

Three compounds TNZ, TNZBr and TNZCHO were synthesized by adopting simple one- and two-step Suzuki reactions. The reference TNZ is reported according to the previous literature. To investigate the influence of introducing the heavy atom effect and intramolecular charge transfer (ICT) effect on the ROS efficiency and ROS species, the bromine atom (Br) and benzaldehyde group were introduced to TNZ to obtain targeted compounds TNZBr and TNZCHO, respectively. Nuclear magnetic spectra (NMR) were measured to confirm their

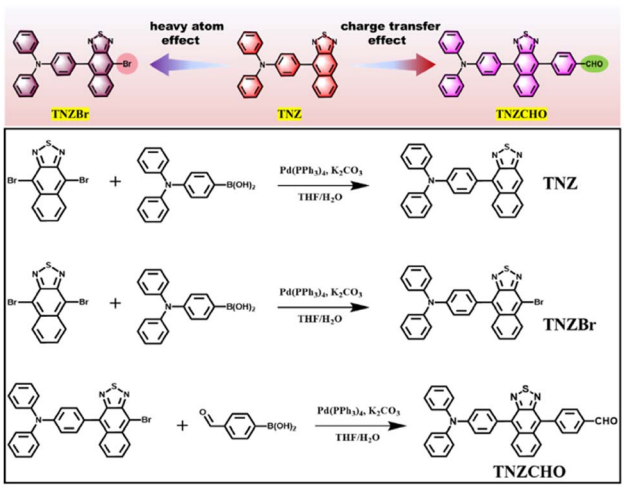

Scheme 1 Synthetic routes for TNZ, TNZBr and TNZCHO.

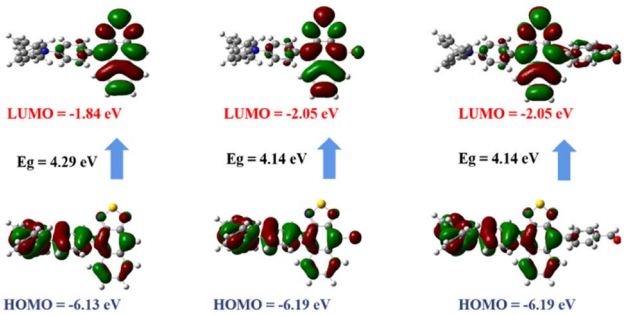

Fig. 1 Electronic cloud distribution of HOMOs and LUMOs at the ground state determined at the M0-62X/6-31G(d,p) level.

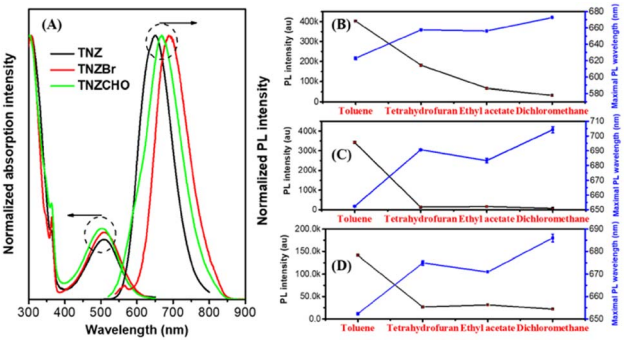

Fig. 2 (A) Absorption and fluorescence spectra of TNZ, TNZBr and TNZCHO in THF solution. Change in the emitted fluorescence intensity and maximal emission wavelength in various solvents with different polarities: (B) TNZ, (C) TNZBr, and (D) TNZCHO. Concentration of emitters: 10 μM.

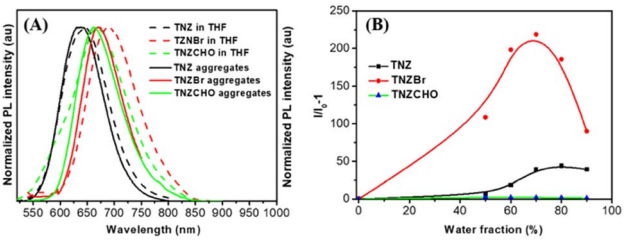

Fig. 3 (A) Fluorescence spectra of TNZ, TNZBr and TNZCHO in THF solution and the aggregated state (90% water fraction in DMSO/H_2O mixture). (B) Change in the emitted fluorescence intensity in DMSO/H_2O mixtures with different water fractions. Concentration of emitters: 10 μM.

molecular structure (Fig. S1–S6†), and high-resolution mass spectrometry (HRMS) was used to measure the molecular weight of TNZBr and TNZCHO (Fig. S15 and S16†); the results suggested the successful preparation of TNZ, TNZBr and TNZCHO.

Fig. 1 presents the theoretical calculations of the electron cloud distribution and energy of highest occupied molecular orbitals (HOMOs) and lowest unoccupied molecular orbitals (LUMOs), which is used to understand the process of electronic transition in depth. In their HOMO frontier orbitals, electrons

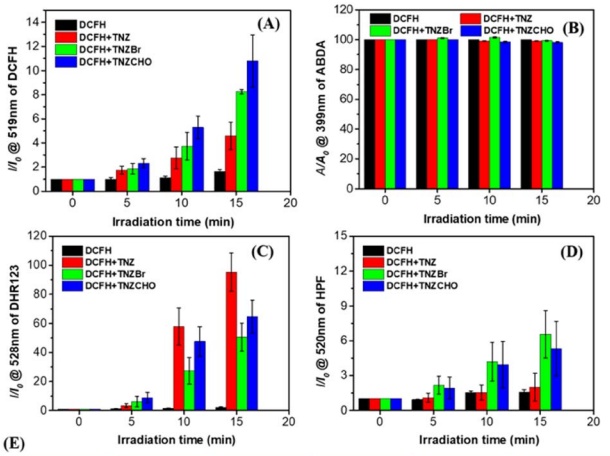

(E)

	S_1 (eV)	S_2 (eV)	T_1 (eV)	T_2 (eV)	$\Delta E_{T2\text{-}S1}$ (eV)
TNZ	2.77	3.37	1.54	3.02	0.25
TNZBr	2.64	3.23	1.46	2.91	0.27
TNZCHO	2.62	3.23	1.47	2.91	0.29

Fig. 4 ROS detection of TNZ, TNZBr and TNZCHO using different ROS probes: (A) H2DCF-DA, (B) ABDA, (C) DHR123, and (D) HPF. (E) Energy levels of the emitters according to theoretical calculations based on TD-DFT.

were mainly distributed on the TNZ skeleton, leading to similar HOMO energy levels (−6.13 eV, −6.19 eV and −6.19 eV). However, differences were observed among LUMOs; for example, the electrons of the LUMO of TNZ were mainly concentrated on the NTZ core and its adjacent benzene ring, while the LUMO electrons of TNZBr and TNZCHO not only concentrated on the NTZ core and its adjacent benzene ring, but also distributed on the Br atom and benzaldehyde group. This difference causes their differences in LUMO energy levels; TNZ has a LUMO energy of −1.84 eV, while the LUMOs of TNZBr and TNZCHO are deeper at −2.05 eV, resulting in a smaller energy gap for TNZBr and TNZCHO than for the reference compound TNZ, suggesting possibly longer absorption and emission wavelengths for TNZBr and TNZCHO than TNZ.

Fig. 2 presents UV-Vis absorption and fluorescence spectra, which were used to verify the correctness of above theoretical calculations and observe absorption and emission peaks. The maximum absorption peaks of the three emitters are located at around 506 nm and are ascribed to the ICT transition from the triphenylamine (TPA) unit to the NTZ core according to theoretical calculations. Adopting their maximum absorption wavelength as the excitation wavelength, their fluorescence spectra were collected. Compared to the TNZ sample with a maximum emission wavelength peaking at 650 nm, TNZCHO and TNZBr show an obvious redshift in their emission maxima, which are located at 667 nm and 691 nm, respectively. This result is in good agreement with the theoretical calculation of smaller energy gaps for TNZCHO/TNZBr than TNZ. Theoretical calculations reveal that the three emitters all have significant ICT behavior from TPA to the NTZ core; therefore, to provide evidence of their ICT properties, a test of the solvent effect on the three emitters was carried out by monitoring the change in

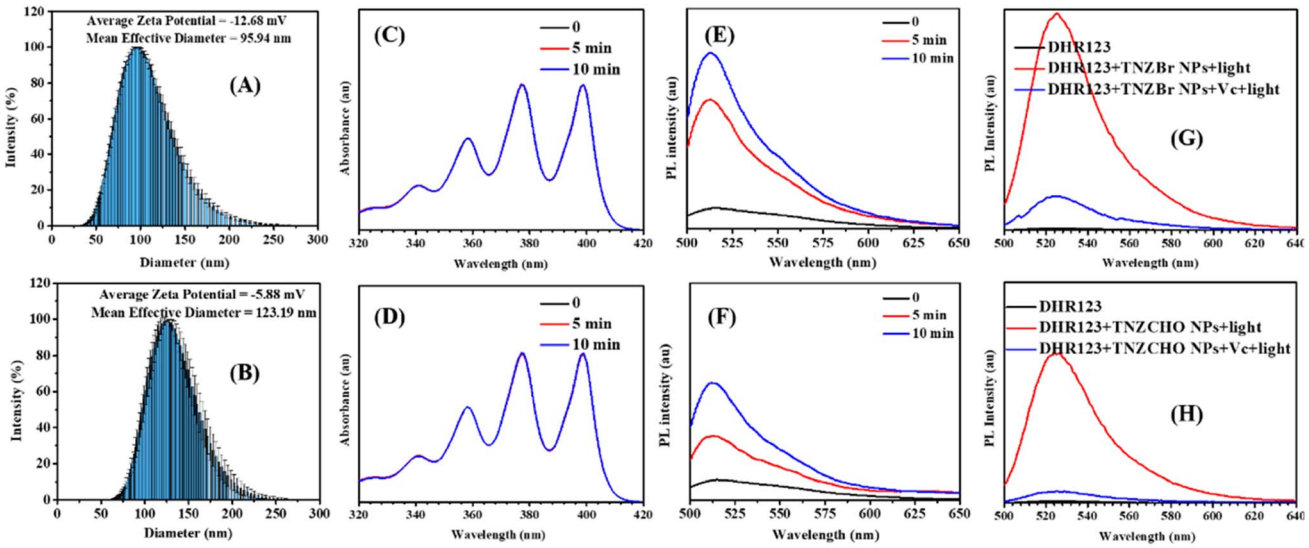

Fig. 5 (A) Dynamic light scatting spectrum of TNZBr NPs and (B) dynamic light scatting spectrum of TNZCHO NPs. (C) Absorption spectra of the ABDA probe in the presence of TNZBr NPs undergoing white light irradiation for different times. (D) Absorption spectra of the ABDA probe in the presence of TNZCHO NPs undergoing white light irradiation for different times. (E) Fluorescence spectra of the HPF probe in the presence of TNZBr NPs undergoing white light irradiation for different times. (F) Fluorescence spectra of the HPF probe in the presence of TNZCHO NPs undergoing white light irradiation for different times. (G) Fluorescence spectra of the DHR probe in the presence of TNZBr NPs undergoing white light irradiation for 10 min. (H) Fluorescent spectra of the DHR probe in the presence of TNZCHO NPs undergoing white light irradiation for 10 min. Light source: 50 mW cm^{-2}, concentration of PS-based NPs: 3.3 μg mL^{-1}.

the fluorescence intensity and maximum emission wavelength in various organic solvents with different polarities. As shown in Fig. 2B–D and S7,† from low-polarity toluene to high-polarity dichloromethane, the maximum emission wavelength of all the emitters was gradually red-shifted, and their fluorescence intensity was quenched when the solvent polarity became larger. This provides solid evidence that the three emitters possess typical ICT features.

Fig. 3 demonstrates the change in fluorescence spectra and intensity from the solution to aggregates. As shown in Fig. 3A, with the formation of aggregates in aqueous solution due to their hydrophobicity, the wavelength of maximum emission peaks decreases compared to the maximum fluorescence wavelength in THF solution. Specifically, TNZ, TNZBr and TNZCHO have maximum fluorescence wavelengths peaking at 648, 687 and 669 nm, respectively, which are blue-shifted to 637, 670 and 661 nm, respectively. This might be ascribed to the environmental polarity decreasing after aggregation comparing that when dissolved in THF solvent. Their AIE performance is further evidenced by measuring the change in fluorescence intensity in the DMSO/H_2O mixture with different water fractions. As shown in Fig. 3B and S8,† in the DMSO solvent, the three emitters all show very weak fluorescence because of the synergistic interactions of the stronger ICT effect and drastic molecular motion to quench fluorescence.[37,38] Once aggregation occurs, molecular motion is suppressed, which weakens the non-radiative transition channel, and more singlet energy can be used to emit fluorescence.[39] In addition, the environmental polarity decreases because formed nano-aggregates could reduce the influence of fluorescence from the DMSO solvent. The photoluminescence quantum yields of TNZBr and TNZCHO in solution and powder were measured. In dimethyl sulfoxide, there is hardly any fluorescence with PLQYs of 0.03% and 0.6%, but they emit obvious fluorescence with PLQYs of 4.0% and 11.4% in powder.

ROS detection

The introduction of stronger ICT and heavy atom effect is beneficial for promoting an intersystem crossing (ISC) channel between singlet and triplet states, resulting in inducing the generation of ROS.[40] To provide evidence for this, Fig. 4 measures and compares clearly the ROS performances of these emitters. First, H2DCF-DA probe was used to detect the total ROS generation upon white light irradiation. As shown in Fig. 4A and S9,† the three emitters could effectively generate ROS, as indicated by the obvious enhancement in fluorescence intensity from the H2DCF-DA probe, and the ability of TNZBr and TNZCHO to generate ROS is higher than that of TNZ, as indicated by their stronger fluorescence signal under the same conditions, suggesting that the introduction of the heavy atom and ICT effect could indeed improve the ROS efficiency of the PSs. To identify the type of ROS generated, the ABDA probe, which shows specific recognition of the type II ROS singlet oxygen ($^1O_2$), was first used. As shown in Fig. 4B and S10,† the absorption intensity of the ABDA probe shows little change even when a mixed solution of the PSs and ABDA probe is irradiated with white light for 10 min, demonstrating that there is almost no $^1O_2$ generation. Therefore, type I ROS should be considered. DHR123, a well-known fluorescent indicator that shows bright green fluorescence after interacting with $O_2^{\bullet-}$, was used to detect whether these three PSs could produce the type I ROS

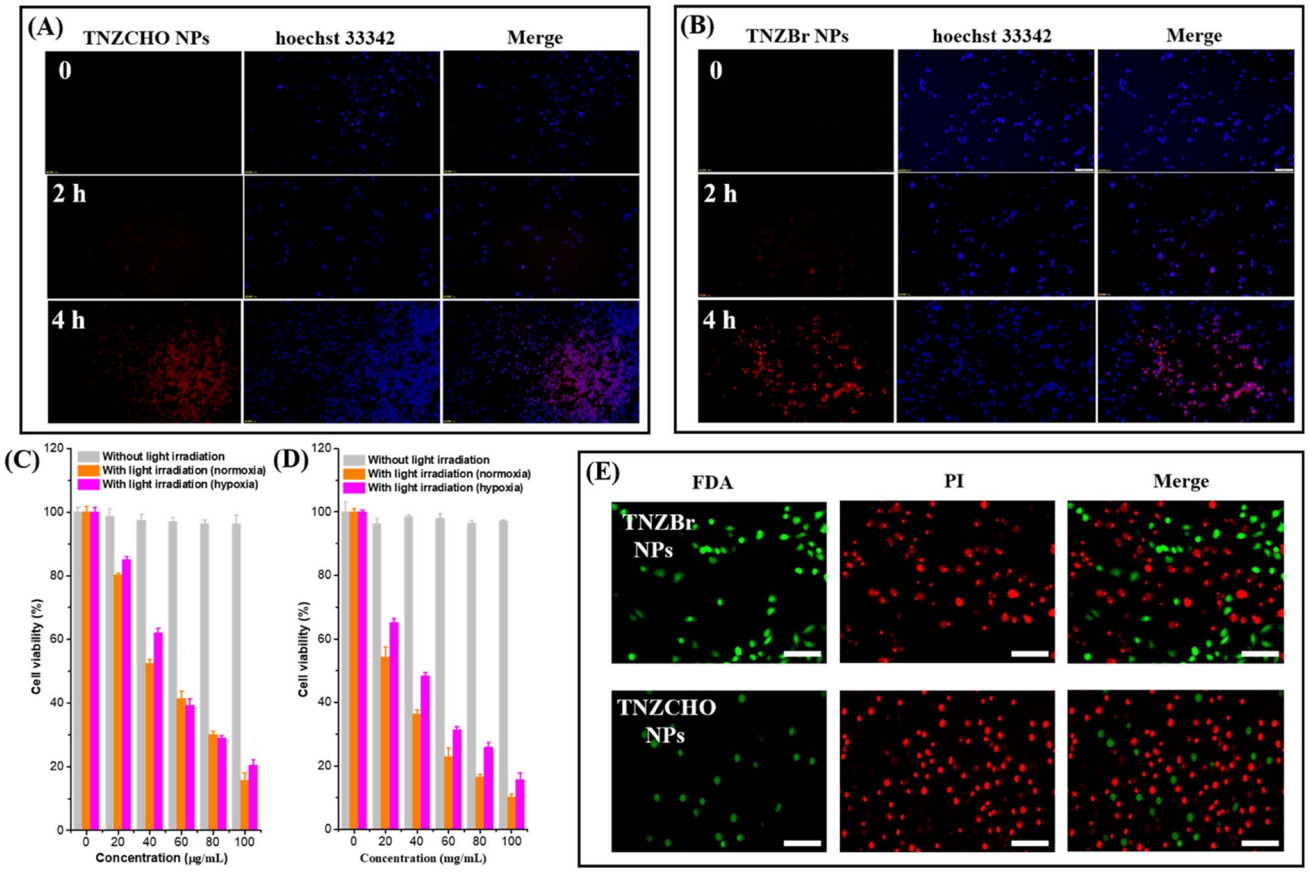

Fig. 6 (A) *In vitro* fluorescence imaging of HUVEC cells using TNZCHO (concentration of 50 μg mL^{-1}). (B) *In vitro* fluorescence imaging of HUVEC cells using TNZBr NPs (concentration of 50 μg mL^{-1}). (C) Cellular viability of TNZCHO-NP-treated HepG2 cells with and without white light irradiation for 10 min. (D) Cellular viability of TNZBr-NP-treated HepG2 cells with and without white light irradiation for 10 min. (E) Confocal microscopic images of HepG2 cells treated with TNZBr NPs or TNZCHO NPs (concentration of 100 μg mL^{-1}, light power of 50 mW cm^{-2}).

$O_2^{\bullet-}$. As shown in Fig. 4C and S11,† upon light irradiation, the fluorescence intensity of the DHR123 probe is obviously enhanced, which suggests that the three PSs could produce the type I ROS $O_2^{\bullet-}$. TNZ results in stronger fluorescence of DHR123 probe than the other two PSs, which could demonstrate that TNZ has better ability to generate $O_2^{\bullet-}$. Finally, another type I ROS, $^{\bullet}OH$, was detected using the specific fluorescent probe HPF. As shown in Fig. 4D and S12,† neither the pure probe nor PS TNZ alone produce significant $^{\bullet}OH$ after suitable light irradiation, as indicated by the lack of obvious enhancement of the fluorescence intensity. In contrast, TNZBr and TNZCHO generated $^{\bullet}OH$ effectively, as shown by the significant enhancement of the fluorescence intensity from the probe. Theoretical calculations of excited energy levels were carried out. As shown in Fig. 4E, the larger energy splitting (ΔE_{st}) between the lowest singlet state (S_1) and lowest triplet state (T_1) demonstrates that intersystem crossing (ISC) from S_1 to T_1 could not occur. However, the ΔE_{st} values of S_1 and T_2 is smaller, being calculated as 0.25 eV, 0.27 eV and 0.29 eV, suggesting a possible ISC process to produce triplet energy in these three PSs.

To improve the hydrophilicity of the PSs TNZBr and TNZCHO, the amphiphilic polymer $DSPEG_{2000}$ was used to encapsulate them to afford polymeric nanoparticles (TNZBr NPs and TNZCHO NPs). The TNZBr NPs and TNZCHO NPs have PLQYs of 2.1% and 9.4%, respectively. Fig. 5 presents the diameters and ROS performance of the TNZBr/TNZCHO-based NPs. First, the absorption and fluorescence spectra of the PS-based NPs were collected. As shown in Fig. S13,† the absorption area of the two NPs covers the entire visible region ranging from 250 to 650 nm, their absorption peak maxima were located at 517 and 536 nm, and their photoluminescence peak maxima were located at 670 nm (Fig. S14†). Such a wide absorption range make these PSs-based NPs better able to absorb the energy from white light, which is good for producing ROS after irradiation with a white light source. Therefore, the efficiency of the TNZBr and TNZCHO NPs for generating ROS was then evaluated. Prior to this, the diameters of the two NPs were measured; the TNZBr and TNZCHO NPs have particle sizes of 95.94 nm and 123.19 nm, respectively, and their surface potentials are −12.68 mV and −5.88 mV, respectively (Fig. 5A and B); these small NPs could enter cells well, theoretically. Next, the ROS properties of the NPs were characterized. As shown in Fig. 5C and D, similarly to the corresponding small molecules, the polymeric NPs do not produce $^1O_2$ after white light irradiation, but could effectively produce the type I ROS

$^{\cdot}OH$ (Fig. 5E and F). The production of another type I ROS, $O_2^{\cdot-}$, was also confirmed by combining the specific probe DHR123 and vitamin C (VC); as shown in Fig. 5G and H, the fluorescence of the DHR123 probe improves obviously when two PS-based NPs solutions are irradiated by white light; however, when VC was added to the aqueous solutions of the PS-based NPs, the fluorescence intensity showed a slight enhancement, which indicates that the two PS-based NPs could generate $O_2^{\cdot-}$.

Cellular imaging and PDT efficiency

Based on their better performances involving bright deep red/near-infrared red fluorescence and effective ROS generation, the TNZBr- and TNZCHO-based NPs were further used for the biological applications of labelling human umbilical vein endothelial (HUVEC) cells and killing HepG2 cancer cells. Fig. 6 presents cellular imaging and PDT effects. As shown in Fig. 6A and B due to their smaller diameter, the TNZCHO NPs could enter HUVEC cells within 4 hours, as demonstrated by the fact that bright red fluorescence could be observed clearly in the cells. In contrast, the TNZBr NPs started to enter the cells within 2 hours, which may be ascribed to the smaller particle size of the TNZBr NPs. The *in vitro* photodynamic therapeutic efficacy of the TNZBr and TNZCHO NPs towards HepG2 cancer cells was investigated using CCK-8 assay. As shown in Fig. 6C and D, both the NPs possess negligible dark cytotoxicity to cells; even at a high concentration of 100 μg mL^{-1}, the cellular viability is still close to 100%. Furthermore, routine blood assays and blood biochemistry tests of healthy mice after receiving an intratumoral injection of the TNZBr NPs or TNZCHO NPs were carried out to further evaluate the biological safety of the two NPs (Fig. S17†). The results show that blood parameters were within their normal ranges, suggesting the good biocompatibility of the NPs. However, under white light irradiation (50 mW cm^{-2}), the two PSs-based NPs exhibit obvious photocytotoxicity to the cancer cells in a dose-dependent manner. In the case of the TNZCHO NPs, the cellular viability decreases to 52.5% after treatment with a concentration of 40 μg mL^{-1} in the normal oxygen environment, reaching 15.6% when the treatment concentration was 100 μg mL^{-1}. For the TNZBr NPs, when cells are treated with a concentration of 40 μg mL^{-1}, the cellular viability decreases to 36.3%, which is further reduced to 10.2% when the concentration of NPs is 100 μg mL^{-1}. Above results demonstrate the effective photocytotoxicity of the TNZBr- and TNZCHO-based PS NPs. Additionally, under a hypoxic environment, TNZBr and TNZCHO still exhibit effective phototherapeutic outcomes. Further, to directly confirm the PDT outcomes, live/dead cell staining experiments were performed using a co-staining assay (fluorescein diacetate (FDA)/propidium iodide (PI)). As shown in Fig. 6E, the cancer cells treated with the TNZBr NPs and TNZCHO NPs show bright red fluorescence, with only a small amount of green fluorescent cells being retained, suggesting the satisfactory phototherapeutic efficacy of the two PS-based NPs toward the cancer cells. In the hypoxic condition, the PDT efficacy of the two NPs is obviously effective toward the cancer cells (Fig. S18†).

Conclusions

In summary, we designed and prepared three PSs with bright NIR fluorescence *via* a very simple synthetic process. Through introducing the heavy atom and ICT effects, a fluorescence red shift occurred, and the ROS efficiency was obviously enhanced. An investigation of the ROS performance of PSs demonstrates that TNZBr and TNZCHO produce only type I ROSs including $O_2^{\cdot-}$ and $^{\cdot}OH$, without producing any type II ROS $^1O_2$. *In vitro* bioimaging results reveal that the PSs could achieve clear fluorescent visualization of HUVEC cells, as well as good phototherapeutic efficacy towards HepG2 cells under normal and hypoxic conditions. This work develops a simple method to prepare NIR-type PSs that exhibit satisfactory efficacy for the fluorescence imaging of HUVEC cells and anticancer effect toward HepG2 cells. In addition, we propose some possible factors for the design of type I PSs based on our results: (1) smaller energy gap between the molecular T_1 state and ground state ($\Delta E_{T_1-S_0}$), which could suppress the energy transfer channel between triplet energy and oxygen; (2): electron-rich environment around the PS, which is beneficial for accelerating electron transfer to produce type I ROS; (3) longer lifetime of the T_1 state, which provides enough reactive time for electron transfer from the electron to the T_1 state to occur; (4) creating a strong ICT and heavy atom effect to boost the efficiency of type I ROS production.

Author contributions

Dr Z. Y. Li was associated with biological experiments and ROS detection, Dr Y. L. Xie and Dr Q. Wan were associated with materials preparation, structure characterization and financial support. J. Wang, G. Wang, H. X. Wang, X. J. Su, M. X. Lei contributed to the checking of this paper, Prof. Y. L. Zhou and Prof. M. Z. Teng provided the idea and financial support.

Conflicts of interest

There are no conflicts to declare.

Acknowledgements

This work is supported by the Gansu Provincial Natural Science Foundation (21JR11RA121 and 23JRRA1518), Special fund for laboratory animals of Gansu Natural Science Foundation (23JRRA1014), Project of Gansu Provincial Department of Education (2023QB-056), Talent Innovation and Entrepreneurship Project of Lanzhou City (2022-RC-49), Talent Innovation and Entrepreneurship Project of Chengguan District (2022-rc-7) and Natural Science Foundation of Jiangxi Province (20224BAB214001 and 20232BAB203026).

Notes and references

1 S. Mitsuhashi, *J. Int. Med. Res.*, 1993, **21**, 1–14.
2 L. J. Li, Q. Chong, L. Wang, G. B. Cher and R. A. Soo, *J. Thorac. Dis.*, 2020, **12**, 3785–3795.

3 H. Zhou, D. Tang, Y. Yu, L. Zhang, B. Wang, J. Karges and H. Xiao, *Nat. Commun.*, 2023, **14**, 5350.
4 K.-X. Teng, L.-Y. Niu and Q.-Z. Yang, *J. Am. Chem. Soc.*, 2023, **145**, 4081–4087.
5 T. E. Kim and J.-E. Chang, *Pharmaceutics*, 2023, **15**, 2257.
6 Q. Wan, R. Zhang, Z. Zhuang, Y. Li, Y. Huang, Z. Wang, W. Zhang, J. Hou and B. Z. Tang, *Adv. Funct. Mater.*, 2020, **30**, 2002057.
7 Y. Sun, X. Geng, Y. Wang, X. Su, R. Han, J. Wang, X. Li, P. Wang, K. Zhang and X. Wang, *ACS Pharmacol. Transl. Sci.*, 2021, **4**, 802–812.
8 J. Zhao, R. Huang, Y. Gao, J. Xu, Y. Sun, J. Bao, L. Fang and S. Gou, *ACS Mater. Lett.*, 2023, **5**, 1752–1759.
9 P. Sivasakthi and P. K. Samanta, *J. Phys. Chem. A*, 2023, **127**, 8900–8910.
10 A. Akbar, S. Khan, T. Chatterjee and M. Ghosh, *J. Photochem. Photobiol., B*, 2023, **248**, 112796.
11 H. Zhang, G. Ren, W. Hou, L. Wang, Y. Sun and J. Liu, *Spectrochim. Acta, Part A*, 2024, **308**, 123688.
12 G. G. Köse and A. Erdoğmuş, *Photochem. Photobiol.*, 2024, **100**, 52–66.
13 S. Liu, G. Feng, B. Z. Tang and B. Liu, *Chem. Sci.*, 2021, **12**, 6488–6506.
14 Y. Li, Q. Wu, M. Kang, N. Song, D. Wang and B. Z. Tang, *Biomaterials*, 2020, **232**, 119749.
15 S. Wang, X. Wang, L. Yu and M. Sun, *Photodiagn. Photodyn. Ther.*, 2021, **34**, 102254.
16 Q. Wan, Y. Li, K. Ding, Y. Xie, J. Fan, J. Tong, Z. Zeng, Y. Li, C. Zhao, Z. Wang and B. Z. Tang, *J. Am. Chem. Soc.*, 2023, **145**, 1607–1616.
17 Z. Cong, S. Xie, Z. Jiang, S. Zheng, W. Wang, W. Wang and H. Song, *Chem. Eng. J.*, 2022, **431**, 133748.
18 Y. Huang, D. Li, D. Wang, X. Chen, L. Ferreira, M. C. L. Martins, Y. Wang, Q. Jin, D. Wang, B. Z. Tang and J. Ji, *Biomaterials*, 2022, **286**, 121579.
19 Z. Liu, Q. Wang, W. Qiu, Y. Lyu, Z. Zhu, X. Zhao and W.-H. Zhu, *Chem. Sci.*, 2022, **13**, 3599–3608.
20 M. Li, Y. Shao, J. H. Kim, Z. Pu, X. Zhao, H. Huang, T. Xiong, Y. Kang, G. Li, K. Shao, J. Fan, J. W. Foley, J. S. Kim and X. Peng, *J. Am. Chem. Soc.*, 2020, **142**, 5380–5388.
21 M. Li, J. Xia, R. Tian, J. Wang, J. Fan, J. Du, S. Long, X. Song, J. W. Foley and X. Peng, *J. Am. Chem. Soc.*, 2018, **140**, 14851–14859.
22 M. Li, T. Xiong, J. Du, R. Tian, M. Xiao, L. Guo, S. Long, J. Fan, W. Sun, K. Shao, X. Song, J. W. Foley and X. Peng, *J. Am. Chem. Soc.*, 2019, **141**, 2695–2702.
23 M. Kang, Z. Zhang, W. Xu, H. Wen, W. Zhu, Q. Wu, H. Wu, J. Gong, Z. Wang, D. Wang and B. Z. Tang, *Adv. Sci.*, 2021, **8**, 2100524.
24 Y. Xie, Z. Li, C. Zhao, R. Lv, Y. Li, Z. Zhang, M. Teng and Q. Wan, *Luminescence*, 2024, **39**, e4621.
25 H. Chen, Y. Wan, X. Cui, S. Li and C.-S. Lee, *Adv. Healthcare Mater.*, 2021, **10**, 2101607.
26 S. Chatterjee, Y. Ie, M. Karakawa and Y. Aso, *Adv. Funct. Mater.*, 2016, **26**, 1161–1168.
27 P. Wei, L. Duan, D. Zhang, J. Qiao, L. Wang, R. Wang, G. Dong and Y. Qiu, *J. Mater. Chem.*, 2008, **18**, 806–818.
28 L. Bu, J. Chen, X. Wei, X. Li, H. Ågren and Y. Xie, *Dyes Pigm.*, 2017, **136**, 724–731.
29 J. Li, Z. Zhuang, Z. Zhao and B. Z. Tang, *View*, 2022, **3**, 20200121.
30 D. Chen, Q. Xu, W. Wang, J. Shao, W. Huang and X. Dong, *Small*, 2021, **17**, 2006742.
31 D. Chen, Q. Yu, X. Huang, H. Dai, T. Luo, J. Shao, P. Chen, J. Chen, W. Huang and X. Dong, *Small*, 2020, **16**, 2001059.
32 J. An, S. Tang, G. Hong, W. Chen, M. Chen, J. Song, Z. Li, X. Peng, F. Song and W. Zheng, *Nat. Commun.*, 2022, **13**, 2225.
33 J. Tian, B. Li, F. Zhang, Z. Yao, W. Song, Y. Tang, Y. Ping and B. Liu, *Angew. Chem., Int. Ed.*, 2023, **62**, e202307288.
34 W. Chen, Y. Zhang, H. Yi, F. Wang, X. Chu and J. Jiang, *Angew. Chem., Int. Ed.*, 2023, **62**, e202300162.
35 T. Xiong, Y. Chen, Q. Peng, S. Lu, S. Long, M. Li, H. Wang, S. Lu, X. Chen, J. Fan, L. Wang and X. Peng, *Adv. Mater.*, 2024, **36**, 2309711.
36 K. Wen, H. Tan, Q. Peng, H. Chen, H. Ma, L. Wang, A. Peng, Q. Shi, X. Cai and H. Huang, *Adv. Mater.*, 2022, **7**, 2108146.
37 Z. Zhao, H. Zhang, J. W. Y. Lam and B. Z. Tang, *Angew. Chem., Int. Ed.*, 2020, **59**, 9888–9907.
38 Y. Hong, J. W. Y. Lam and B. Z. Tang, *Chem. Soc. Rev.*, 2011, **40**, 5361–5388.
39 J. Zou, Z. Yin, K. Ding, Q. Tang, J. Li, W. Si, J. Shao, Q. Zhang, W. Huang and X. Dong, *ACS Appl. Mater. Interfaces*, 2017, **9**, 32475–32481.
40 F.-Z. Xu, C.-Y. Wang, Q. Wang, J.-W. Zou, Y.-J. Qiao, Z.-Q. Guo, W. Zhao and W.-H. Zhu, *Chem. Commun.*, 2022, **58**, 6393–6396.